

Coherent Structures Governing Transport at Turbulent Interfaces

Ali R Khojasteh, Lyke E. van Dalen, Coen Been,
Jerry Westerweel and Willem van de Water¹

¹*Laboratory for Aero- and Hydrodynamics,
Delft University of Technology and J.M. Burgers Centre
for Fluid Dynamics, 2628 CD Delft, The Netherlands**

(Dated: 12 December 2024)

Abstract

In an experiment on a turbulent jet, we detect interfacial turbulent layers in a frame that moves, on average, along with the turbulent-nonturbulent interface. This significantly prolongs the observation time of scalar and velocity structures and enables the measurement of two types of Lagrangian coherent structures. One structure, the finite-time Lyapunov field (FTLE), quantifies advective transport barriers of fluid parcels while the other structure highlights barriers of diffusive momentum transport. These two complementary structures depend on large-scale and small-scale motion and are therefore associated with the growth of the turbulent region through engulfment or nibbling, respectively. We detect the turbulent-nonturbulent interface from cluster analysis, where we divide the measured scalar field into four clusters. Not only the turbulent-nonturbulent interface can be found this way, but also the next, internal, turbulent-turbulent interface. Conditional averages show that these interfaces are correlated with barriers of advective and diffusive transport when the Lagrangian integration time is smaller than the integral time scale. Diffusive structures decorrelate faster since they have a smaller timescale. Conditional averages of these structures at internal turbulent-turbulent interfaces show the same pattern with a more pronounced jump at the interface indicative of a shear layer. This is quite an unexpected outcome, as the internal interface is now defined not by the presence or absence of vorticity, but by conditional vorticity corresponding to two uniform concentration zones. The long-time diffusive momentum flux along Lagrangian paths represents the growth of the turbulent flow into the irrotational domain, a direct demonstration of nibbling. The diffusive flux parallel to the turbulent-nonturbulent interface appears to be concentrated in a diffusive superlayer whose width is comparable with the Taylor microscale, which is relatively invariant in time.

* Corresponding author: A.R.Khojasteh@tudelft.nl

I. INTRODUCTION

A turbulent flow can be viewed as regions of uniform momentum separated by interfacial layers where the gradient of vorticity fluctuates strongest [1–5]. In jet flow, the outermost of these layers is known as the turbulent-nonturbulent interface, which separates rotational (turbulent) and irrotational regions, and is characterized by a sharp change in flow properties [6, 7]. At the interface, non-turbulent fluid is incorporated into the turbulent region, by both large scale and small scale processes, referred to as ‘engulfment’ and ‘nibbling’ respectively. Numerical and experimental findings indicated that the entrainment process is predominantly a small-scale process, with engulfment contributing only slightly in the self-similar region of the jet [6–9]. Figure 1 illustrates the current state of affairs, and sketches the focus of the present article. Engulfment involves fluid motion on large scales, while small-scale vortices, concentrated in a vortical superlayer [1], dominate the spread of the turbulence into the irrotational domain. In Figure 1(b), the flow of enstrophy stops at the turbulent-nonturbulent interface, but the small-scale vortices propel the flow of viscous momentum $\mu\nabla^2\mathbf{u}$. While engulfment and nibbling have so far been studied in the Eulerian frame, we emphasize their Lagrangian context. It inspired the design of our quasi-Lagrangian setup where the detection of velocity and scalar fields moves with the average interface velocity. Figure 1(c) illustrates two (complementary) quantities of interest in this paper: the backward-in-time rate of separation (Λ) of two fluid parcels, and the convergence (Ψ) of viscous momentum flux $\mu\nabla^2\mathbf{u}$. These Lagrangian structures are typically defined for a finite time T . In this paper these times *precede* the instant of observation.

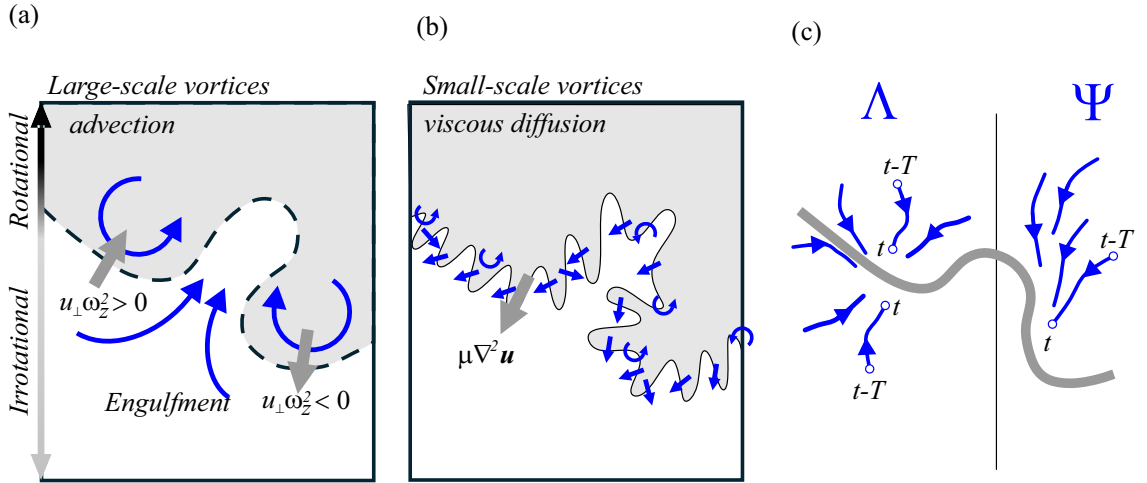


FIG. 1. (a) The turbulent-nonturbulent interface separates irrotational and turbulent flow. A large-scale process, i.e. engulfment, mixes irrotational fluid into the turbulent domain. (b) Small-scale vortices propagate and convolute the turbulent-nonturbulent interface, enabling a diffusive momentum flux $\mu\nabla^2\mathbf{u}$ across the interface. (c) Advection-diffusion at the interface in a Lagrangian frame. The two distinct types of structures considered in this paper are: the finite-time Lyapunov field Λ , i.e. (i) the divergence (in backward time) of fluid parcels that are close at time t , and (ii) the convergence Ψ of streamlines of the diffusive momentum flux. Both quantities are averages along Lagrangian trajectories over a time T preceding the instant of observation.

The state of the art in recent experiments on turbulent interfaces involves the simultaneous measurement of the velocity field using particle-image velocimetry (PIV), while the

concentration field is measured using laser-induced fluorescence (LIF) [10–12]. It enables the detection of the turbulent-nonturbulent interface of a jet seeded with dye and determine its correlation with the velocity field. However, flows at high Reynolds numbers pose a challenge for achieving high spatial resolution, restricting the detail and accuracy of the observations. Furthermore, in most experiments the flows are recorded with stationary cameras, which limits the possibility to track Lagrangian evolution of these interfaces over longer times.

In this work we consider the turbulent-nonturbulent interface of a submerged turbulent round jet exiting into a quiescent volume of fluid at a Reynolds number $\text{Re} \approx 1.25 \times 10^4$. The jet is seeded with dye, which is visualized using LIF, while the velocity field in an axial planar cross section is measured using PIV. A novelty of this experiment is the measurement of the dye concentration and velocity in a frame that moves with the average downstream and radial velocity of the turbulent-nonturbulent interface. Using the statistics of the measured concentration fields, we identify not only the turbulent-nonturbulent interface but also an *internal* turbulent-turbulent interface.

The purpose of this investigation is to relate these interfaces to coherent Lagrangian structures. One particular structure, i.e. the ridge-like local maxima of the finite-time Lyapunov field $\Lambda(\mathbf{x})$, forms a barrier to large-scale advective transport [13–15]. The other structure, $\Psi(\mathbf{x})$, is related to barriers of the diffusive flux of momentum, and thus highlights small-scale structures [16]. Both structures are *objective*: they are independent of the frame of observation [16]. The detection of these structures requires extended observation times in a Lagrangian frame, which necessitates an experimental setup where the detection cameras move along the flow. This provides a substantial enhancement of the spatial resolution of the measured velocity field near the interface over an extended downstream distance. This method avoids limitations in spatial resolution associated with a fixed camera observing the entire jet, as well as scenarios where the camera measures near the interface at a fixed location, which fail to capture the long-time evolution of the interface. The present paper (and our earlier work, [17]) focuses on the time dependence, whereas existing studies involve snapshots only.

The prevalence of small-scale nibbling over large-scale engulfment was concluded on the basis of a small correlation length (of the order of the Taylor microscale) of the velocity fluctuations near the turbulent-nonturbulent interface and the relatively small area of irrotational fluid inside a planar cross section of the jet [6, 7, 9]. As noted by Mathew and Basu [8], the entrainment process is related across scales. Mistry *et al.* [10] formulate a corollary to these results: the turbulent-nonturbulent interface is considered to be a fractal surface, and using filtering with an increasing filter length Δ they conclude that the filtered entrainment velocity increases with increasing Δ , while the filtered surface area decreases with increasing Δ , such that the mass flux (the product of entrainment velocity and area) does not depend on Δ , which was already suggested by Meneveau and Sreenivasan [18].

The turbulent-nonturbulent interface is the boundary between the turbulent (rotational) domain and the nonturbulent (irrotational) domain, which we will sometimes denote as ‘blue sky’ below (as in a white turbulent cloud against a blue sky background). The turbulent-nonturbulent interface is not a material surface and propagates into the irrotational domain with velocity $E_B = -2V$ for a round turbulent jet [19], where V is the velocity of a fluid parcel perpendicular to the interface. The role of viscous and nonviscous effects can be appreciated by considering the propagation velocity E_B of the turbulent-nonturbulent interface. Westerweel *et al.* [6, 9] argue that the entrainment boundary velocity E_B follows from a nonviscous stress balance, $E_B \Delta \tilde{U} \approx -\langle \tilde{u}\tilde{v} \rangle$ (the boundary jump condition), with \tilde{u}, \tilde{v}

fluctuating velocities conditional to the location of the interface, and $\Delta\tilde{U}$ the jump of the mean axial velocity component [9, 20–22]. In this frame the enstrophy does not change and an analysis of the enstrophy transport equation [23, 24] also allows to isolate the viscous contributions to the interface velocity. After all, the initial transport of vorticity away from a body accelerated from rest is through viscous diffusion [25].

While the turbulent-nonturbulent interface separates turbulent from nonturbulent fluid, *internal* interfaces were identified by Eisma *et al.* [5] using thresholds on a velocity gradient tensor [26]. These thin shear layers were first reported by Meinhart and Adrian [2], and subsequently studied in turbulent boundary layers [3, 27, 28]. In all these cases, interfaces were found using measured velocity fields, either by imposing thresholds, or by identifying zones of approximately uniform momentum using PDF's of the instantaneous streamwise velocity.

In the present article we identify interfaces from the scalar field using the well-established techniques of cluster analysis [29, 30]. This is obvious for the turbulent-nonturbulent interface, which separates scalar from the absence of scalar. However, the scalar concentration field towards the core of the jet appears to be organized in uniform concentration zones that can be used to find *internal* boundaries. Specifically, when these zones are ranked according to their concentration level, the turbulent-nonturbulent interface is the boundary between the first two zones, with the first zone the region of unmixed fluid, whereas a turbulent-turbulent interface is a boundary between subsequent zones. We then compute conditional averages of vorticity ω , and the new fields Λ, Ψ on these internal boundaries.

An outline of this paper is as follows: Coherent structures are described in Sec. II. The experimental setup, where we move with the flow, is discussed in Sec. III; it includes a discussion (Sec. III B) of how to interpret results in a moving frame. The detection of the turbulent interfacial layers based on images of dye fluorescence and cluster analysis is described in Sec. IV. Conditional averages on the contorted fractal interfaces are defined in Sec. V. The results are presented in Sec. VI, and finally the conclusions of this work are given in Sec. VII.

II. COHERENT STRUCTURES

We view coherent structures in this work as barriers for either advective or diffusive quantities: manifolds that hinder momentum transport. In the case of diffusive transport, it is possible to quantify the flux across an interface, time averaged along Lagrangian paths, using conditional averages.

The significance of the two Lagrangian structures introduced in figure 1c with respect to the turbulent-nonturbulent interface is as follows: if the transport across the turbulent-nonturbulent interface is carried by large-scale structures, the interface should not be related to barriers of momentum flux. On the other hand, if the growth of the turbulent region is through diffusion of vorticity, the turbulent-nonturbulent interface should not be a barrier to diffusive momentum flux. The possible association with a barrier field is but one aspect of the turbulent-nonturbulent interface. We now briefly describe the two coherent structures that are measured in our experiments.

A. Barriers for advective transport

Finite-time Lyapunov exponents gauge the exponentially fast spreading of nearby fluid parcels. Ridge-like maxima in the finite-time Lyapunov exponent field $\Lambda(\mathbf{x}, t)$ of the associated field $\Lambda(\mathbf{x}, t)$ form barriers for passive tracers [14, 15], which are associated with the large-scale structure of the flow.

The evolution operator (flow map) \mathbf{F} of material points $\mathbf{x}(t)$ that start at \mathbf{x}_0 and are carried by the velocity field $\mathbf{u}(\mathbf{x}, t)$ is defined as

$$\mathbf{x}(t) = \mathbf{F}_{t_0}^t(\mathbf{x}_0) = \int_{t_0}^t \mathbf{u}(\mathbf{x}(t'), t') dt'. \quad (1)$$

Its gradient field $\mathbf{M}_{t_0}^t = \nabla \mathbf{F}_{t_0}^t$ describes the evolution of small separations $\boldsymbol{\delta}$ between fluid parcels. It can be computed from a measured velocity field by integrating the evolution of a vector $\boldsymbol{\delta}$ in the velocity gradient field along a Lagrangian trajectory,

$$\frac{d\boldsymbol{\delta}}{dt} = \mathbf{A}(\mathbf{x}(t), t) \cdot \boldsymbol{\delta}(t), \quad \text{with} \quad \frac{d\mathbf{x}(t)}{dt} = \mathbf{u}(\mathbf{x}, t), \quad \mathbf{A} = \nabla \mathbf{u} \quad \text{and} \quad \mathbf{x}(t = t_0) = \mathbf{x}_0. \quad (2)$$

The largest eigenvalue λ_2 of the positive Cauchy-Green tensor,

$$\mathbf{C}_{t_0}^t = \mathbf{M}_{t_0}^t (\mathbf{M}_{t_0}^t)^\dagger, \quad (3)$$

with $t = t_0 + T$ and with \dagger the adjoint operation, then defines the finite-time Lyapunov field $\Lambda_T(\mathbf{x}_0, t_0)$ as

$$\Lambda_T(\mathbf{x}_0, t_0) = \frac{1}{2|T|} \ln(\lambda_2). \quad (4)$$

Our experimental technique gives access to the planar cross section of the velocity field; consequently, there are only two eigenvalues. In the case $T > 0$, Eq. (3) expresses the separation of fluid parcels that are close at t_0 and separate in the future $t_0 + T$. Similarly, by integrating the trajectories *backward* in time, the largest eigenvalue of $\mathbf{C}_{t_0}^{t_0-T}$ defines the *backward* Lyapunov field $\Lambda_{-T}(\mathbf{x}_0, t_0)$. Reijtenbagh *et al.* [17] found that it was the backward in time field Λ_{-T} that delineated large-scale structure of the scalar field in the core of a jet. We expect that in the irrotational domain the separation remains small, while there a sudden increase occurs when a fluid parcel enters the turbulent flow region. Since the field $\Lambda_{-T}(\mathbf{x}, t)$ is Lagrangian, it is *objective*: it is the same for all observers, independent of their (moving, accelerated) observation frame. To emphasize its ridges, the field Λ_{-T} is filtered to include only regions with negative curvature in the direction of the eigenvector corresponding to λ_2 .

B. Barriers of diffusive momentum transport

In the Navier-Stokes equations the diffusive momentum transport of an incompressible fluid is expressed by the term $\mathbf{h} = \nu \nabla^2 \mathbf{u}$, with ν the kinematic viscosity. As argued by Haller *et al.* [16], the field $\mathbf{h}(\mathbf{x}, t)$ is objective. While \mathbf{h} represents the diffusive *flow* of momentum, its *flux* involves a surface A with surface normal field \mathbf{n} . As time evolves, not only \mathbf{h} changes, but also the surface A and the surface normal field \mathbf{n} are carried along with

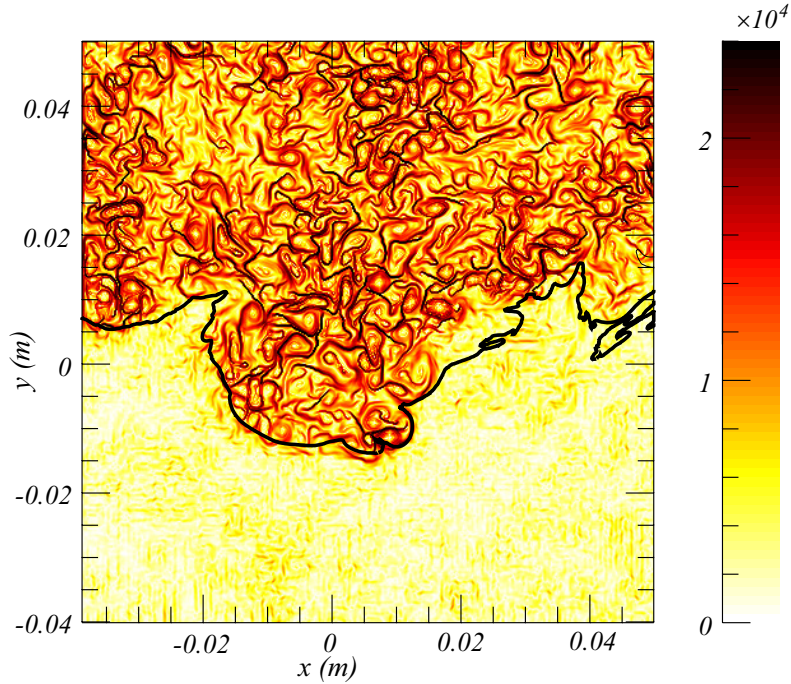


FIG. 2. Snapshot of the diffusive flux field Ψ_0 ; the solid line represents the turbulent-nonturbulent interface as defined by the fluorescent dye. The quantity Ψ_0 provides a clear identification of the turbulent flow region that closely corresponds to the turbulent flow region marked by the dyed fluid that originally left the jet nozzle.

the fluid parcels. Using an elementary result of mechanics [31], the infinitesimal contribution to the flux at time t is related to that at time t_0 through

$$\mathbf{h}(\mathbf{x}, t) \cdot \mathbf{n} \, dA = \det [\nabla \mathbf{F}_{t_0}^t] \underbrace{[\nabla \mathbf{F}_{t_0}^t]^{-\dagger} \mathbf{h}(\mathbf{F}_{t_0}^t(\mathbf{x}_0), t)}_{\mathbf{b}_{t_0}^t(\mathbf{x}_0)} \cdot \mathbf{n}_0 \, dA_0, \quad (5)$$

where dA_0 and \mathbf{n}_0 are the infinitesimal surface area and its normal, respectively, at an initial time t_0 . In incompressible 3D flow $\det [\nabla \mathbf{F}_{t_0}^t] = 1$, which we also adopt for convenience, although we only have 2D information. The vector $\mathbf{b}_{t_0}^t$ embodies the time dependence of the flux contribution of fluid parcels that start at \mathbf{x}_0 at time t_0 and flow through the infinitesimal surface that has evolved from time t_0 to time t . The flux contribution, averaged over the Lagrangian path that is traveled from $t = t_0$ to $t = t_0 + T$, then involves the time averaged vector $\bar{\mathbf{b}}_{t_0}^{t_0+T}$,

$$\bar{\mathbf{b}}_{t_0}^{t_0+T} = \frac{1}{|T|} \int_0^T \mathbf{b}_{t_0}^{t_0+t'} \, dt'.$$

The vector field $\bar{\mathbf{b}}_{t_0}^{t_0+T}$ can be defined for both forward ($T > 0$) and backward ($T < 0$) times. Surfaces that block diffusive momentum transport come with streamlines of $\bar{\mathbf{b}}_{t_0}^{t_0+T}$ that are tangent to them. Conversely, the convergence or divergence of streamlines of $\bar{\mathbf{b}}_{t_0}^{t_0+T}$ delineates barriers of diffusive momentum transport. These properties can be found from the gradient field $\nabla \bar{\mathbf{b}}_{t_0}^{t_0+T}$ in much the same fashion as was discussed in Sec. II A; technicalities

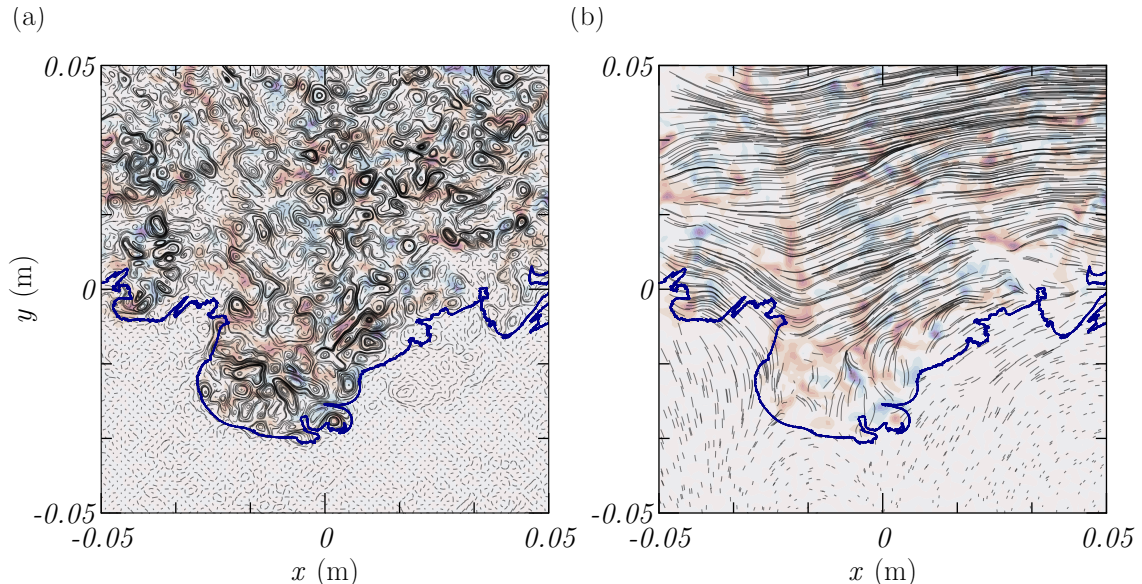


FIG. 3. Instantaneous streamlines (a) the diffusive momentum flux and (b) advective transport of tracer particles. The blue line represents the turbulent-nonturbulent interface.

are detailed below in Sec. VIC. The associated field is called $\Psi_T(\mathbf{x}, t)$. Summarizing, the vector field $\bar{\mathbf{b}}_{t_0}^{t_0+T}$ is the natural way to express the time-averaged flux of diffusive momentum. Its properties can be studied directly, e.g. through its streamlines, or $\bar{\mathbf{b}}_{t_0}^{t_0+T}$ can be used to measure the flux through turbulent interfaces.

It is possible to characterize in the same way the *instantaneous* flux, $\mathbf{b}_{t_0}^{t_0} = \nu \nabla^2 \mathbf{u}(\mathbf{x}_0, t_0)$. As Fig. 2 shows, the field Ψ_0 sharply defines the boundary between the turbulent and the irrotational domains, even more acutely than the vorticity field ω_z (as shown in Fig. 5). This is remarkable as the diffusive momentum flow \mathbf{h} is trivially related to the vorticity field: in incompressible 2D flow, i.e. $\nabla \cdot \mathbf{u} = 0$, \mathbf{h} is explicitly given by ω_z , $\mathbf{h} = \nu \nabla^2 \mathbf{u} \equiv \nu(-\partial\omega_z/\partial y, \partial\omega_z/\partial x)$.

While ridge-like local maxima of Λ_T are barriers of large-scale flow, the structures Ψ_T emphasize the diffusive flux of momentum. The vector field $\bar{\mathbf{b}}_{t_0}^{t_0+T}(\mathbf{x})$ can be computed from a measured velocity field in much the same fashion as the finite-time Lyapunov field. While Λ_T involves the gradient velocity field \mathbf{A} , a measurement of $\nabla^2 \mathbf{u}$ takes one more derivative. It is regularized by averaging $\bar{\mathbf{b}}_{t_0}^t$ over a time T , but the gradient matrix $\nabla \mathbf{F}_{t_0}^t$, which strongly fluctuates along Lagrangian paths, now adds to the noise. However, turning the vector field $\bar{\mathbf{b}}_{t_0}^{t_0+T}$ into Ψ_T significantly enhances its signal to noise ratio.

Fig. 3 illustrates instantaneous transport streamlines resulting from the advective transport of passive tracers (\mathbf{u}) and the diffusive transport of linear momentum ($\nu \nabla^2 \mathbf{u}$). As soon as integration time goes above zero time, these streamlines change in time and become pathlines. The finite-time Lyapunov exponent acts as an operator on these pathlines to identify ridges that define Lagrangian coherent structures. Advective streamlines primarily stretch along the dominant advection direction and also transport across the interface (see Fig. 3). Diffusive streamlines, on the other hand, form small-scale structures irrespective of the main flow direction.

III. EXPERIMENTAL SETUP

Water seeded with a fluorescent dye (rhodamine-6G) flows through a 10 mm diameter jet nozzle with nominal velocity of 1.25 m/s. The flow through the nozzle is controlled and emanates in the water-filled test section of a water channel with a $0.60 \times 0.60 \text{ m}^2$ cross section and a length of 5.0 m. The jet Reynolds number is $\text{Re} = (1.25 \pm 0.03) \times 10^4$, which is above the mixing transition ($\text{Re} \approx 10^4$) [32]. The dissipation rate ε is estimated from $\varepsilon = 0.015 U_c^3 / L$ [33], where U_c is the local mean centerline velocity of the jet, and L the jet half-width. This gives a Kolmogorov length scale of $\eta = 0.20 \text{ mm}$ at the start of the measurement (at $x = 0.53 \text{ m}$ from the nozzle exit), and a Taylor length scale of $\lambda_T = 4.9 \text{ mm}$. The detection of concentration and velocity is designed to move with the turbulent-nonturbulent interface. The x, y -traverse system is driven by two stepper motors (MDrive23Hybrid, Schneider Electric, USA), with a 2 m span along the x -axis parallel to the jet axis, and a 1 m span in the y -direction. The jet characteristics vary with the distance x to the nozzle, and are detailed in Fig. 4(b). The flow in the test section is illuminated with a thin laser light sheet with a thickness of 1.5 mm, generated from a dual pulsed Nd:YAG laser (Spectra-Physics PIV-400). Detection of the dye concentration (using LIF) and flow velocity (using PIV) fields involve two high-resolution sCMOS cameras (LaVision Imager CLHS) operating at a framing rate of 15 Hz, with the double frames separated by 4 ms exposure time. The LIF image corresponds to the first PIV frame. The LIF camera is positioned 0.1 m above the PIV camera and tilted downwards by 3 degrees to match the field of view of the PIV camera (see Fig. 4(a)). We mount a long-pass filter (SCHOTT OG570) on the LIF camera and a 525 nm bandpass filter (TECHSPEC) on the PIV camera. Both cameras use 105 mm lenses. We use a calibration grid and an image mapping function to overlay the two measurement fields with an error of less than 0.2 pixels.

The cameras move at a constant velocity of 0.02 m/s and a 9 degree angle with respect to the jet axis as shown in Fig. 4(d). However, the interface velocity decreases as a function of the downstream location. This means that at the start of the traverse, the interface velocity is higher, but it becomes lower than the traverse velocity toward the end. As a compromise, we considered only the part of the traverse where both velocities match (see Fig. 4.(b)). The cameras have a common field of view of $100 \times 120 \text{ mm}^2$ with a scale factor of 0.05 mm/px. The LIF camera only records the light emitted from the rhodamine dye using an optical long-pass filter, while the PIV camera records the light scattered off spherical hollow glass particles, allowing for simultaneous LIF and PIV measurements with an aperture number $f^\#$ of 5.6. A scalar calibration was done to ensure a linear relation between the dye concentration $\varphi(\mathbf{x}, t)$ and the observed fluorescence intensity. In the remainder of this paper φ is expressed in intensity counts.

A. Analysis of LIF and PIV images

The 2105×2563 -pixel LIF images are filtered using a Gaussian width of 4 pixels (standard deviation $(4/2)^{1/2}$ pixels) and subsequently downsampled to 508×638 -pixel images. Filtering reduces photon noise but at the expense of spatial resolution. The resulting equivalent pixel size in the object plane is $2 \times 10^{-4} \text{ m}$, which is approximately the estimated average value of the Kolmogorov length η at the beginning of the region of interest. It should be compared to the 1.5 mm width of the light sheet and the vector spacing $\approx 10^{-3} \text{ m}$ of the measured velocity field. Occasionally, dust particles may light up or fluorescent dye reflected off the

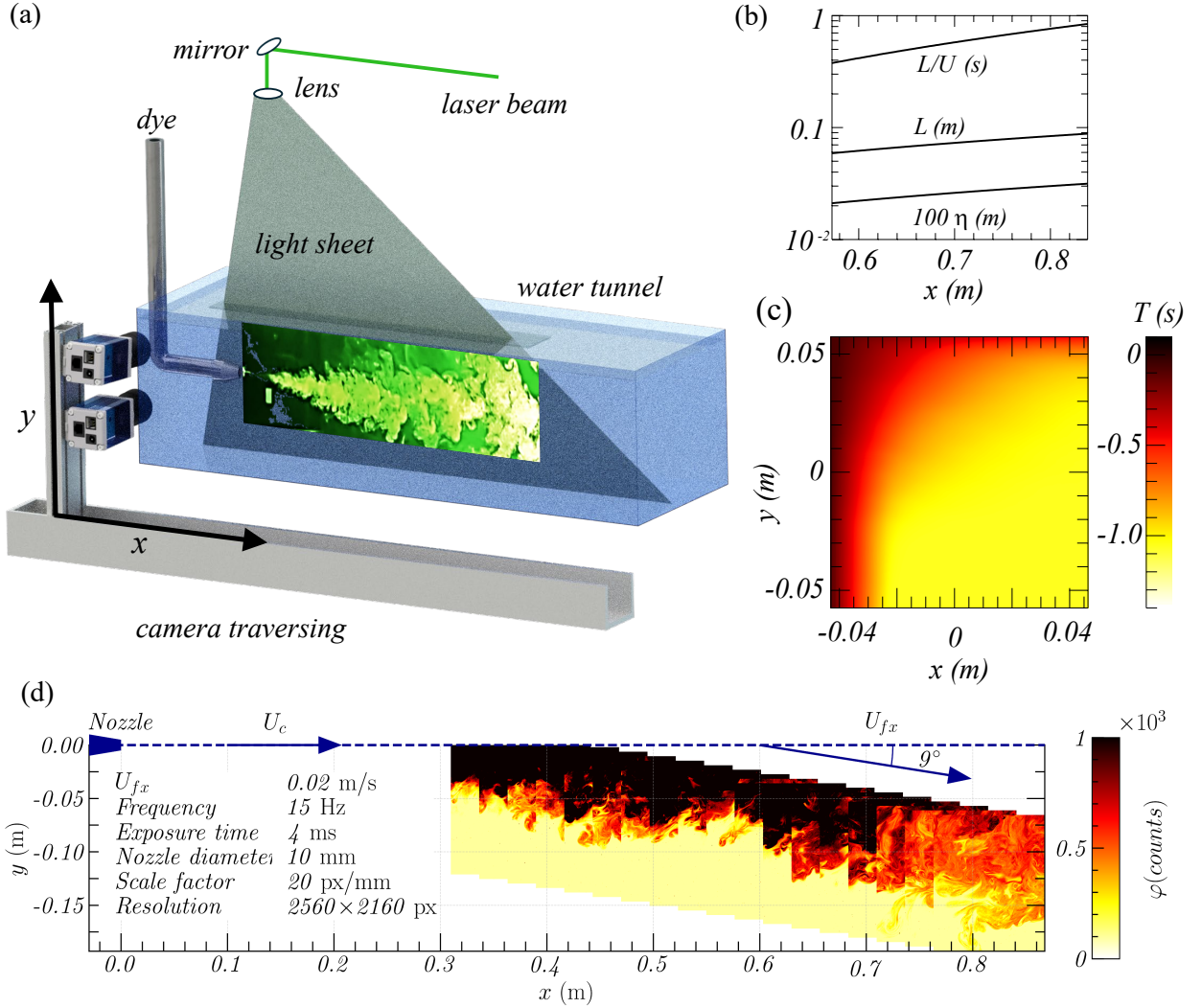


FIG. 4. Experiment characteristics. (a) The PIV and LIF cameras move with the turbulent-nonturbulent interface. The horizontal component of the frame traverse velocity U_{fx} is 2 cm/s, and points 9° downward. (b) Variation over the region of interest of relevant length and time scales, where L is the local jet half-width, U_c the local mean velocity at the jet centerline, and η the local Kolmogorov scale; L/U_c is the local integral time scale. (c) Average residence time of fluid parcels within the field-of-view trajectories backwards in time (i.e., $T < 0$). In the upper half of the frame, the observation time is limited by the higher velocities towards the jet centerline, while on the left side of the frame, quiescent fluid outside the jet exits the field-of-view during the motion of the cameras. (d) The concentration fields of a single run as a function of global coordinates.

particles in the LIF images, which causes cluster analysis to fail. These spots, leading to isolated peaks at the highest intensity in histograms, were removed from the images using a median filter and replaced by an average over background pixels. The results in this paper are from 200 images in each run, which span the 0.57×0.84 m² region of interest, with x the distance from the nozzle, and taken with a frame rate of 15 Hz. Averages are over 15 repeated runs.

Two-dimensional sections of the velocity field are measured using a multigrid PIV algorithm with rectangular interrogation windows [34], tailored to the large variation of the fluid velocity over the region of interest. The initial size of the interrogation regions is 256×64 -pixel, and the final square size 32×32 -pixel with 50% overlap. The velocity field from PIV is finally evaluated on a grid of 113×145 interrogations, with a spacing of 7.7×10^{-4} m. The frame velocity ($U_{fx} = 2 \times 10^{-2}$ m/s, $U_{fy} = -3.2 \times 10^{-3}$ m/s) is added to the flow velocity; see Sec. III B).

B. Moving with the flow

Moving at the interface's average velocity allows the evolution of flow structures within the field of view to be frozen, in contrast to stationary measurements where structures enter and exit the field of view (see figure 5). There are several ways to interpret experiments in which the detection involves a moving frame of reference. They affect the appearance of Lagrangian tracks $\mathbf{x}(t)$, which in the laboratory frame follow from

$$\frac{d\mathbf{x}}{dt} = \mathbf{u}(\mathbf{x}, t). \quad (6)$$

Let \mathbf{x} and $\mathbf{u}(\mathbf{x}, t)$ be the position and velocity, respectively, in the laboratory frame, and \mathbf{x}' and $\mathbf{u}'(\mathbf{x}', t)$ those in the moving frame. In the present case frame moves with a constant velocity \mathbf{U}_f , so that $\mathbf{x}' = \mathbf{x} - \mathbf{U}_f t$.

One way, as is done here, is to add the frame velocity to the velocity in the laboratory frame,

$$\mathbf{u}'(\mathbf{x}', t) = \mathbf{u}(\mathbf{x}', t) + \mathbf{U}_f, \quad (7)$$

so that $\mathbf{x}' = \mathbf{x}$. Lagrangian trajectories, measured in the moving frame, then follow from

$$\frac{d\mathbf{x}'}{dt} = \mathbf{u}'(\mathbf{x}', t) - \mathbf{U}_f, \quad (8)$$

with $\mathbf{u}' = \mathbf{u} + \mathbf{U}_f$; this is exactly the equation in the laboratory frame. A stationary fluid parcel in the laboratory frame now also has zero velocity in the moving frame. An alternative interpretation is to use the information in the moving frame 'as is', but then the Lagrangian trajectories no longer represent those in the laboratory frame.

We trace fluid parcels backward in time ($T < 0$). The observation time in the moving frame is shown in Fig. 4(d). A small velocity of fluid parcels at the very left edge of the moving frame is the cause that their observation time $|T|$ is small. It is also small near the core of the jet, and it is large at the interface location. The third component of the velocity, which corresponds to out-of-plane motion, is estimated to move particles away from the field of view after 1.5 local integral time at the beginning of the traverse and 0.8 local integral time at the end, at the interface location.

IV. IDENTIFYING THE TURBULENT INTERFACES

The demarcation between zero and finite values of the enstrophy (the turbulent-nonturbulent interface) requires a threshold value ω_{thr}^2 of the enstrophy. In the simulations of Er *et al.*

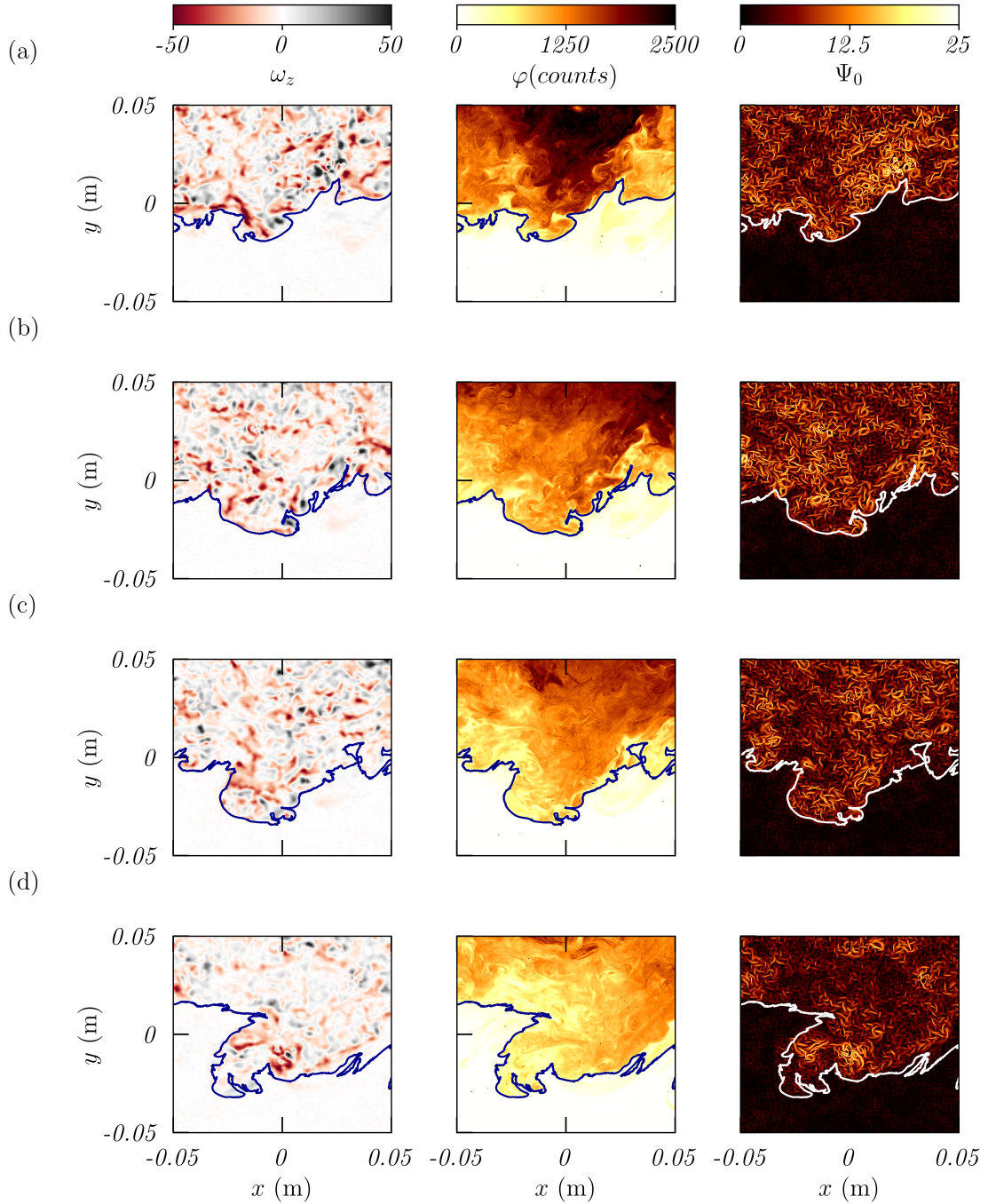


FIG. 5. Quasi-Lagrangian evolution of flow structures at the turbulent-nonturbulent interface (a) to (d) sequential evolution of an engulfment event quantified with vorticity ω_z , scalar φ , and diffusive barrier Ψ_0 .

[35], who took care of numerical oscillations in the region of quiescent fluid, the interface location was found insensitive to ω_{thr}^2 over a large dynamic range ($10^{-8} \lesssim \omega_{\text{thr}}^2 \lesssim 10^{-2}$). In the context of experiments, inevitably influenced by noise, the determination of a threshold is more ambiguous, and the threshold levels are not robust.

The measured scalar concentration field $\varphi(\mathbf{x}, t)$, i.e. the observed fluorescence, is taken

as a proxy of the vorticity, which in two dimensions satisfies the same equation as $\varphi(\mathbf{x}, t)$, but with a negligible diffusivity, so that the dye can effectively be considered as a passive tracer that follows the motion of the fluid elements that passed through the nozzle.¹

We illustrate the identification of the turbulent-nonturbulent interface based on scalar concentration. Ideally there is dye in the seeded turbulent jet, and no dye outside (the ‘blue sky’). However, after repeated runs the region of unmixed fluid may become contaminated by a low background concentration φ_{bg} . Then, the turbulent-nonturbulent interface is the boundary between the region with φ_{bg} and the domain with larger concentration.

It appears that in a turbulent jet flow seeded with dye there are more distinct concentration levels than just these two. The scalar concentration field appears to be organised in uniform concentration zones, i.e. regions where the concentration variation is small [36]. Various approaches exist to identify the boundaries between these regions; here these uniform concentration zones are identified by cluster analysis. This well-established statistical technique [29] arranges the pixels containing concentration values into clusters, as illustrated in Fig. 6. Fan *et al.* [30] originally used this approach to find turbulent interfaces. The optimization procedure uses no spatial information. Although the choice of the number of clusters n_c can be done automatically [37], we take $n_c = 4$; this is the minimum number of clusters to include the identification of the ambient fluid and up to 3 internal uniform concentration zones.

Each cluster has its own concentration distribution; these are shown in Fig. 6(c). The concentration level of an interface is taken as the intersection between the corresponding distributions for each cluster. For the turbulent-nonturbulent interface and the turbulent-turbulent interface these concentration values are φ_{tnti} and φ_{tti} , respectively. Finally, the interfaces are drawn as contours at these concentration values. The essence of the clustering algorithm is an optimal association of concentration values with a small number of clusters. As Fig. 6(c) illustrates, these associations may overlap. An interface marks a jump of the concentration value; those jumps are illustrated in Fig. 6(b). Clearly, identifying those jumps is aided essentially by the clustering algorithm.

Closed contour loops, which correspond to patches of dye that appear unconnected to the turbulent domain, and loops encircling patches of irrotational fluid inside turbulence were removed. In the used contouring algorithm [38], contours come in pieces, of which we kept the 6 longest ones. Occasionally, patches of dye are found on the irrotational side to the turbulent-nonturbulent interface; this is jet fluid that was detrained before the instant of observation, since the camera, that on average follows the edge of the jet, moves at a velocity that is much smaller than the core region of the jet. It is verified that these patches do not contain vorticity.

Our method should be compared to the popular procedure in which the contour level φ_{tnti} is determined from an inflection point in the cumulative distribution of the pixel intensities [39]. We found that this approach does not always yield an unambiguous threshold value. In contrast, once the number of clusters n_c is set, this ambiguity is no longer present in our method. Clusters increasingly overlap with increasing n_c . The first two intensity distributions in Fig. 6(c) are well separated but the definition of the second turbulent-turbulent interface in Fig. 6(a) is less acute (Threshold values of clusters are shown as tickers on the colorbar).

¹ For the dye used in this experiment (rhodamine 6G, $\mathbb{D} = 2.8 \times 10^{-10} \text{ m}^2/\text{s}$), the Schmidt number $\text{Sc} = \nu/\mathbb{D}$, with ν the kinematic viscosity and \mathbb{D} the molecular diffusivity, is $\text{Sc} = 3.6 \times 10^3$. Therefore, the Batchelor scale $\eta_B = \eta/\sqrt{\text{Sc}} \cong 3.5 \times 10^{-6} \text{ m}$ remains unresolved.

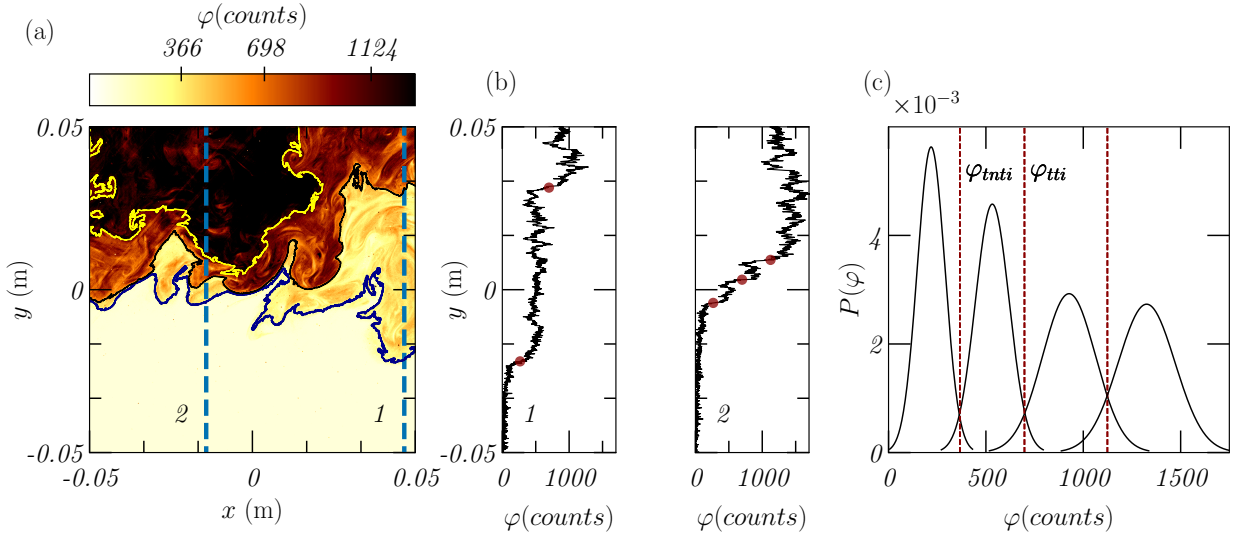


FIG. 6. Detecting the turbulent-nonturbulent interface using cluster analysis. (a) Fluorescence image intensity $\varphi(\mathbf{x}, t)$ (expressed in pixel counts). The lower side of the black line is the turbulent-nonturbulent interface, the upper side is a turbulent-turbulent interface. (b) Concentration profiles along the blue vertical lines (1,2) in (a). The red dots indicate the contour concentration values φ_{tnti} and φ_{tti} that define the turbulent-nonturbulent interface and turbulent-turbulent interface, respectively. Concentration values are subtracted from the background and shifted to have a nonturbulent part starting from zero. (c) Cluster distributions of the pixel intensity levels corresponding to the 4 uniform concentration zones. The red dashed lines indicate the intersection φ_{tnti} between the first and second clusters, and φ_{tti} between the second and third clusters. Contours at the corresponding concentration values are drawn in (a). A second turbulent-turbulent interface is also drawn in (a). Its concentration level follows from the intersection of the third and fourth clusters.

Cluster analysis of the concentration field provides a natural way to find turbulence interfaces as the edges of clusters. Internal turbulence interfaces in a turbulent boundary layer were studied by Eisma *et al.* [5]. Their detection required the distinction of turbulence levels, which was done on the basis of the shear vorticity [26]. Using the scalar field, turbulent-turbulent interfaces were studied by Chen and Buxton [12], with a dyed turbulent wake evolving in background turbulence. In their case, the turbulent-turbulent interface is the interface between turbulence with dye, and turbulence without dye. In contrast, our turbulent-turbulent interface is the interface between two non-zero concentration levels. Below we present conditional averages of ω_z , Λ , and Ψ both on the turbulent-nonturbulent interface and on this turbulent-turbulent interface.

V. CONDITIONAL AVERAGES

The turbulent interfaces are found from the measured dye concentration. To establish the relation with the scalar fields $\omega_z(\mathbf{x}, t)$, $\Lambda_{-T}(\mathbf{x}, t)$, $\Psi_{-T}(\mathbf{x}, t)$, and $\Psi_0(\mathbf{x}, t)$, we use the conditional average as presented by Bisset *et al.* [40]. The question is whether structures of a scalar quantity are aligned with an interface. If so, the conditional average of the scalar

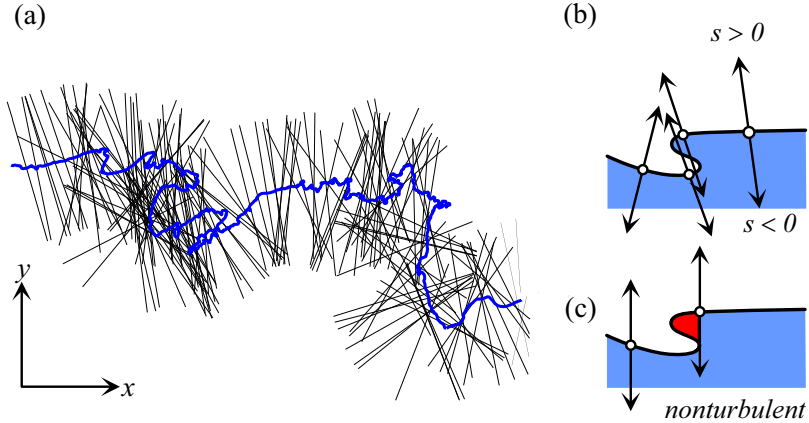


FIG. 7. Conditional averages. (a) The blue curve represents a turbulent-nonturbulent interface, black lines: edge normals $s\mathbf{e}_{\text{tnti}}$. The interface folds back on itself: (b) intersections for edge normal $s\mathbf{e}_{\text{tnti}}$; (c) vertical intersections $s\mathbf{e}_y$ for turbulent-nonturbulent interface outer and inner envelopes, which either include or exclude the red patch of nonturbulent fluid.

should vary sharply at this interface, and should be structureless anywhere else.

The conditional average $\widetilde{\omega}_z(s)$ of the vorticity component ω_z with respect to the turbulent-nonturbulent interface location \mathbf{x}_{tnti} is defined as

$$\widetilde{\omega}_z(s) = \langle \omega_z(\mathbf{x}_{\text{tnti}} + s\mathbf{e}_{\text{tnti}}) \rangle_{\mathbf{x}_{\text{tnti}}},$$

with the unit vector \mathbf{e}_{tnti} directed perpendicularly to the turbulent-nonturbulent interface \mathbf{x}_{tnti} , and where $s < 0$ is the irrotational domain while $s\mathbf{e}_{\text{tnti}}$ with $s > 0$ points into the turbulent domain. In this paper, the tilde symbol (e.g., $\widetilde{\omega}$) denotes a scaled, non-dimensionalized quantity. Averages $\langle \dots \rangle$ are done over the interface, and over all frames and all experiment runs. The conditional average of other scalar quantities is defined analogously. The experimental data is not free of noise so that $\widetilde{\omega}_z(s < 0)$ would still be finite, and even more so for $\widetilde{\Psi}_{-T}$ and $\widetilde{\Psi}_0$.

We define an interface normal intersection \mathbf{e}_{tnti} by first fitting lines to \mathbf{x}_{tnti} with length $\Delta = 16\eta$. Edge normals \mathbf{e}_{tnti} are the bisectors of these lines. A typical result for the normals \mathbf{e}_{tnti} on the turbulent-nonturbulent interface is shown in Fig. 7(b). In choosing edge normals, the interface is covered with boxes with size $\ell_{\text{box}} = 16\eta$, with one intersecting point in each nonempty box. Consequently, the density of edge normals is high where the interface is very contorted, which biases conditional averages. This procedure respects the fractal character of the interface shape. It is well known that the interface has fractal properties [10, 12, 18, 35, 39, 41], with the number of nonempty boxes diverging faster than ℓ_{box}^{-1} with decreasing box size ℓ_{box} .

An alternative choice of intersections is to take the unit vector \mathbf{e}_{tnti} in the *vertical* direction \mathbf{e}_y [6]. This approach needs a procedure to deal with sections where the interface folds back on itself, as illustrated in Fig. 7(b,c), and where the turbulent-nonturbulent interface is chosen as either the outer or inner envelope of the nonturbulent domain. The choice made – to include engulfed irrotational fluid – introduces a bias in the conditional average. In a few cases in Sec. VIA we demonstrate the effect of these choices and find that this bias is small most of the time.

Taking perpendicular cross sections along \mathbf{e}_{tnti} presents a challenge for very contorted interfaces. A few examples are sketched in Fig. 7(c), where the line $s\mathbf{e}_{\text{tnti}}$ may intersect the

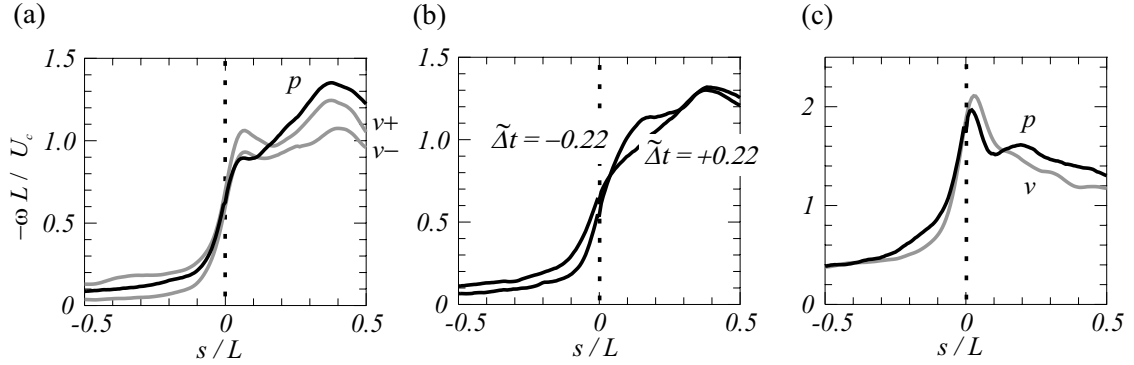


FIG. 8. Conditional averages of the out-of-plane component ω_z of the vorticity. (a) Averages over normal (p) and vertical (v_{\pm}) intersections of the turbulent-nonturbulent interface. The v_{\pm} averages distinguish two envelopes: v_- is the envelope of the nonturbulent domain, as is illustrated in Fig. 7, while v_+ is the envelope of the turbulent domain. (b) Influence of the time delay Δt between the scalar fields $\varphi(\mathbf{x}, t)$ and $\omega(\mathbf{x}, t + \Delta t)$, and thus between perpendicular intersections of the turbulent-nonturbulent interface at t , and ω_z at $t + \Delta t$. The time shift $\tilde{\Delta t}$ is expressed in units of L/U_c (at $x = 0.71$ m). A delay $\tilde{\Delta t}$ then corresponds to two frames. (c) Conditional average with respect to the turbulent-turbulent interface (notice the change of the vertical scale).

turbulent domain several times. If s is the coordinate along the intersection, it is assured that the turbulent domain corresponds to $s > 0$ and $s < 0$ is the region of unmixed fluid. This is done by computing the integrated scalar concentration $\varphi^+ = \int_0^{+\ell/2} \varphi(\mathbf{x}_{\text{tnti}} + s \mathbf{e}_{\text{tnti}}) ds$, and similarly for φ^- , and choosing the sign of s such that $\varphi^+ > \varphi^-$. Intersecting lines with $|\varphi^+ - \varphi^-| / (\varphi^+ + \varphi^-) < 0.1$ are deemed ambiguous and excluded from the conditional average. Before averaging individual sections, the coordinate s is scaled with the jet half width, whose variation during a run is shown in Fig. 4(c). In the case of multiple intersections further refinements are possible, such as only including intervals of s , $s > 0$, in the conditional average that actually correspond to the turbulent domain, and *vice versa* for the irrotational region. These refinements do not significantly change our results. Conditional averages with respect to the turbulent-turbulent interface are done analogously: the sign of s is again chosen such that $\varphi^+ > \varphi^-$.

VI. RESULTS

A. Conditional averages of ω_z

Fig. 8 shows conditional averages of ω_z , where Fig. 8(a) illustrates the two choices of conditional averages on vertical intersections of the turbulent-nonturbulent interface. Both choices either take the envelope of the turbulent domain or take the envelope of the nonturbulent region result in different conditional averages. They both differ from the conditional averages along (perpendicular) edge normals. In the remainder of this paper, we take averages along the proper edge normals of the turbulent interfaces. The result in Fig. 8 can be compared to the result of Mistry *et al.* [10], which is for $|\omega_z|$ at a Reynolds number $e = 2.5 \times 10^4$.

The conditional average of ω_z in Fig. 8(b) depends on the time delay Δt between the

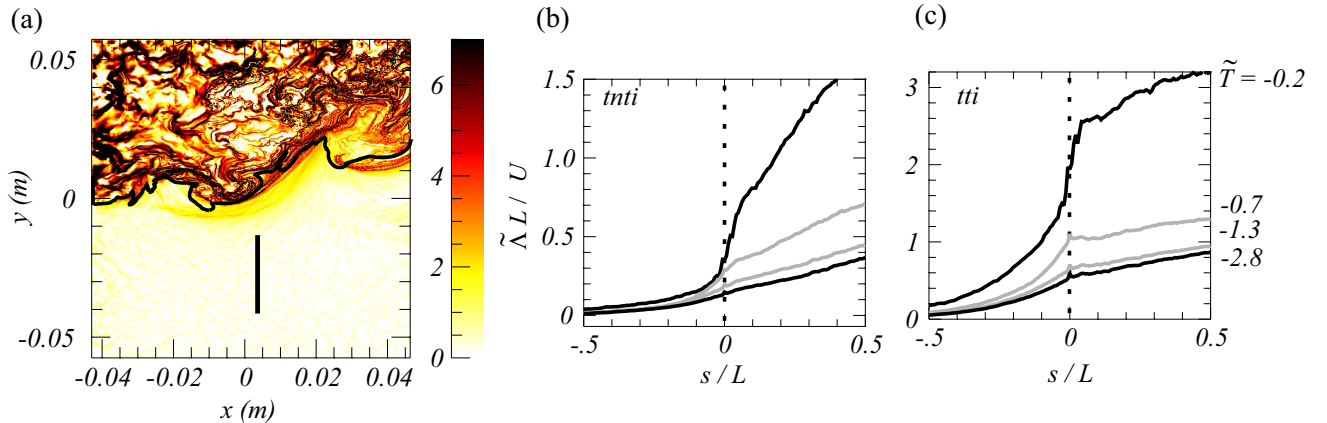


FIG. 9. (a) Snapshot of the field Λ_{-T} for $T = -2.8L/U_c$. The black curve represents the turbulent-nonturbulent interface as detected from the fluorescent dye. The vertical bar indicates the extent of the horizontal axis for $-0.5 \leq s/L \leq +0.5$ in panels (b,c). (b) Conditional averages of Λ_{-T} along normals on the turbulent-nonturbulent interface for a range of (backward) integration times $-T$ expressed in $L/U_c = 0.38$ s. (c) Same as panel (b), but now for the turbulent-turbulent interface. For the curves in (b,c) the asymptote for $s \ll -L$ (i.e., into the irrotational domain) is set to 0.

scalar fields $\varphi(\mathbf{x}, t)$ and $\omega_z(\mathbf{x}, t + \Delta t)$, and thus on the time delay between the turbulent-nonturbulent interface at t and ω_z at $t + \Delta t$. The jump of $\tilde{\omega}_z$ is largest at $\tilde{\Delta t} = -0.22$. The result might illustrate causality: it is the *past* velocity field that has shaped the passive scalar field φ and the turbulent-nonturbulent interface that is obtained from φ .

Conditional averages with respect to the turbulent-turbulent interface are shown in Fig. 8(c); this result shows a more significant jump of the conditional vorticity across the turbulent-turbulent interface, as well as a more pronounced peak that is indicative of a shear layer at the turbulent-turbulent interface [9]. This is a rather surprising result, since this internal interface is no longer defined as one between vorticity and its absence, but between two levels of conditional vorticity associated with two distinct levels of scalar concentration. This result of an increased turbulence level yielding a more pronounced jump in conditional averages agrees with the findings of Eisma *et al.* [5] in a turbulent boundary layer.

B. Conditional averages of Λ_T

In the following figures we show a snapshot of the barriers to the advective field (the first one of the 1.6×10^3 frames taken) together with the conditional averages, both on the turbulent-nonturbulent interface and the turbulent-turbulent interface. The quantitative results of the conditional averages are based on all frames in all repeated runs. Of course, the frames in a single run are not statistically independent. The choice for backward times is inspired by the results of Reijtenbagh *et al.* [17] who found a relation with the edges of uniform concentration zones.

We show snapshots of the Lyapunov field Λ_{-T} and the diffusive flux field Ψ_{-T} at $T = -2.8L/U_c$. For the conditional averages, the (backward) integration times varied from $T = -0.2L/U_c$ to $T = -2.8L/U_c$, with the time scale $L/U_c = 0.38$ s now taken at the start ($x = 0.57$ m) of a run. The actual integration times are limited by the residence time

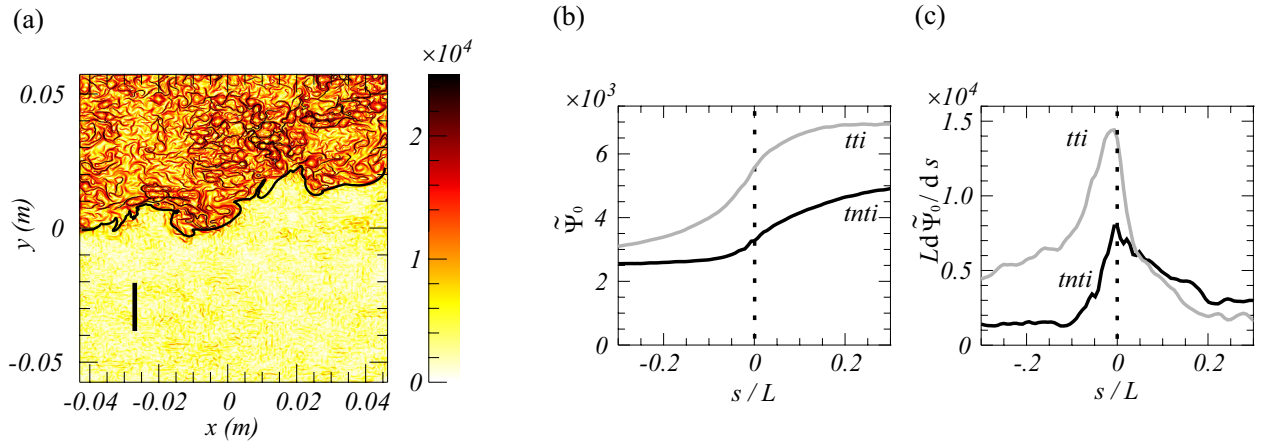


FIG. 10. Conditional averages of Ψ_0 . (a) Snapshot of the zero-time diffusive barrier field Ψ_0 ; the black line represents the turbulent-nonturbulent interface detected from the fluorescent dye. The vertical bar indicates the extent of the horizontal axis for $-0.3 \leq s/L \leq +0.3$ in panels (b) and (c). (b) Conditional average of Ψ_0 over perpendicular intersections of the turbulent-nonturbulent interface and turbulent-turbulent interface. (c) Slopes of the curves in panel (b) sharply peak at the interface locations.

of fluid parcels in the moving observation frame; see Fig. 4(c).

Fig. 9(a) shows an example of the Lyapunov field Λ_{-T} . Since the integration time T depends on the location in the frame, longer integration times result in sharper features when barriers remain invariant in time. Since the traversing velocity of the cameras is set to follow the turbulent-nonturbulent interface, the features of Λ_{-T} (and Ψ_{-T}) become increasingly blurred towards the core of the jet.

The conditional averages of Λ_{-T} along the local normal directions of the turbulent-nonturbulent interface are shown in Fig. 9(b). The dependence on the normal distance s to the turbulent-nonturbulent interface suggests a correlation between the finite-time Lyapunov field and the turbulent-nonturbulent interface, especially for the shorter integration times. The correlation decreases with increasing T , and appears to reach an asymptote at the longest integration time. At that time, the correlation is weaker than the correlation with the vorticity field. These trends appear to be much stronger for conditional averages with respect to the turbulent-turbulent interface, which are shown in Fig. 9(c).

C. Conditional averages of Ψ_0 and Ψ_{-T}

Before discussing the diffusive barrier fields Ψ_{-T} and Ψ_0 , we detail some technicalities. Visualization of the associated structures requires the integration of a dynamical system. For the equal-time diffusive barrier field $\Psi_0(\mathbf{x}_0, t_0)$ we have

$$\frac{d\mathbf{x}}{d\xi} = \mathbf{h}(\mathbf{x}(\xi); t_0), \quad \text{with: } \mathbf{h} = \nu \nabla^2 \mathbf{u}, \quad \text{and: } \mathbf{x}(\xi = 0; t_0) = \mathbf{x}_0, \quad (9)$$

where the active variable (dimensionless ‘pseudo time’) ξ is a curvilinear coordinate, and t_0 is a parameter that represents the physical time at which the structure of $\mathbf{h}(\mathbf{x}_0, t_0)$ is computed. The evolution of the vector field $\mathbf{x}(\xi)$ over a (pseudo) time interval Ξ can be described by a

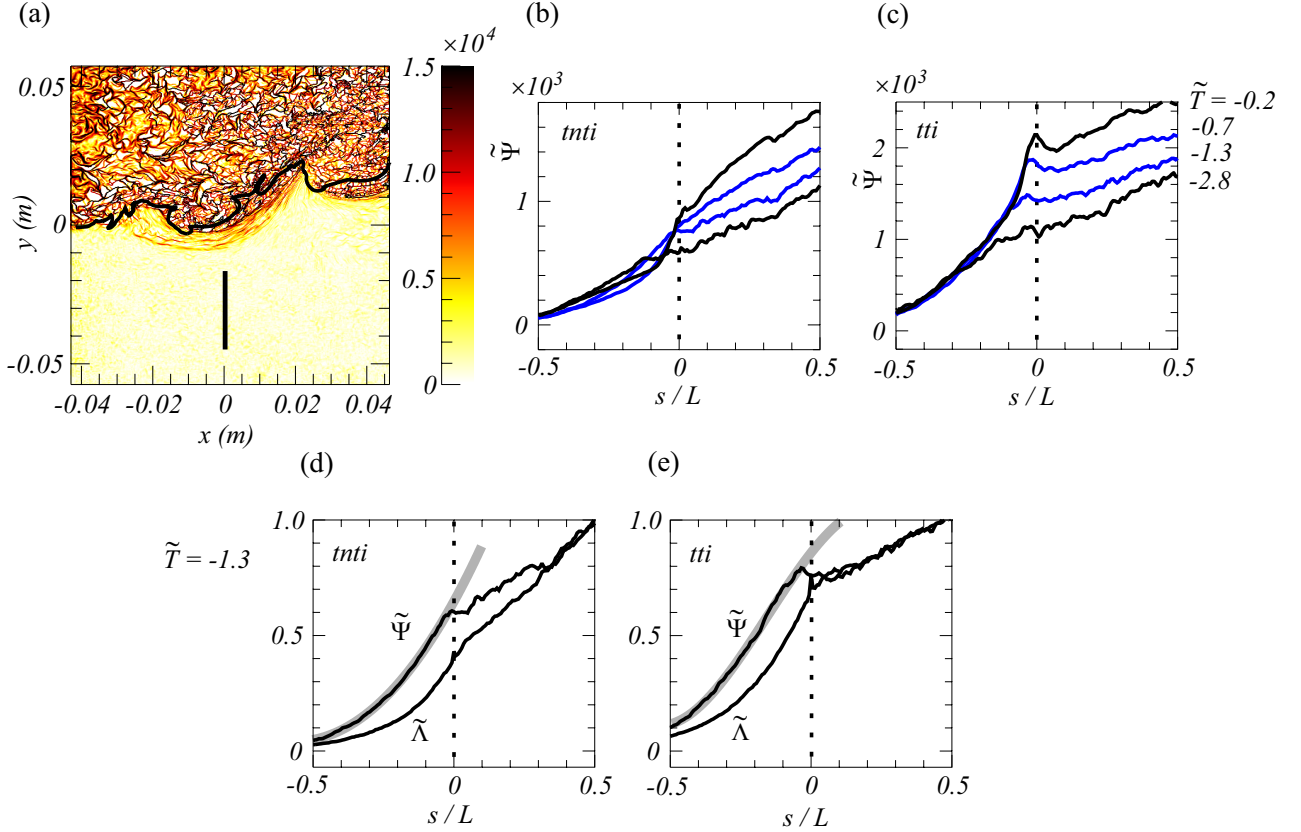


FIG. 11. (a) Diffusive barrier field Ψ_{-T} . The black curve represents the turbulent-nonturbulent interface detected through the fluorescent dye. The vertical bar indicates the extent of the horizontal axis for $-0.5 \leq s/L \leq +0.5$ in panels (b-e). (b) Conditional average of Ψ_{-T} over normal sections of the turbulent-nonturbulent interface for a range of (backward) integration times $-T$, expressed in $L/U = 0.38$ s. The curves asymptote to a background value for $s \ll -L$; this value was subtracted. (c) Same as (b), but for the turbulent-turbulent interface. (d) Normalized conditional averages Ψ_{-T} and Λ_{-T} on the turbulent-nonturbulent interface at $\tilde{T} = 1.3$. The normalization is such that the asymptote at small s is set to 0 and the value at $\tilde{s} = 0.5$ is set to 1. (e) Same as (d), but for the turbulent-turbulent interface. The gray lines are polynomial fits to guide the eye that become linearly dependent on s for $s \geq 0$.

flow map $\mathcal{F}: \mathbf{x}(\Xi) = \mathcal{F}_0^\Xi(\mathbf{x}(0))$. Much as in the case of the finite-time Lyapunov exponent, its gradient $\mathbf{M}_0^\Xi = \nabla \mathcal{F}_0^\Xi$ defines a Cauchy-Green tensor $\mathbf{C}_0^\Xi = \mathbf{M}_0^\Xi (\mathbf{M}_0^\Xi)^T$. The diffusive barrier field Ψ_0 is the logarithm of its largest eigenvalue. The numerical integration of Eq. (9) is done over $\Xi = 2.5 \times 10^{-4}$, corresponding to a displacement $\Delta x = 1.4 \times 10^{-4}$ m, where $\nabla \mathbf{h}$ is computed from finite differences.

From the appearance of Fig. 2, which displays interesting small scale structures, the effort of integrating a dynamical system for visualization, which may look cumbersome at first sight, is worthwhile.

The zero-time field Ψ_0 and its conditional average are shown in Fig. 10, with a larger view already shown in Fig. 2. Since Ψ_0 involves the computation of a second derivative, the noise in the irrotational domain is now larger than that of $\tilde{\omega}_z$. Despite this elevated noise level, the field Ψ_0 sharply defines the turbulent domain indicating that Lyapunov operator

amplifies the signal to noise ratio. Clearly, the representation Ψ , which entails the curvature properties of the streamlines of the vector field $\bar{\mathbf{b}}_t$, has a regularizing effect.

Compared to the conditional vorticity, the conditional average $\tilde{\Psi}_0$ lacks the impression of a ‘superlayer’ [6]. Much as for the vorticity, conditional averages with respect to the turbulent-turbulent interface show a larger jump across the interface.

The finite-time diffusive flux field Ψ_{-T} is shown in Fig. 11(a). Compared to the zero-time field Ψ_0 it involves the time-averaged vector field $\bar{\mathbf{b}}_t^{t_0+T}$, which is visualized in the same way as the field $\mathbf{h}(\mathbf{x}, t) = \nu \nabla^2 \mathbf{u}(\mathbf{x}, t)$ in the case of Ψ_0 . The conditional average in Fig. 11(b) evolves into a featureless asymptote for increasing integration times T . In comparison with the conditional average of the advective barrier field Λ_{-T} field in Fig. 9, $\tilde{\Psi}_{-T}$ reaches its asymptote at shorter times T . The faster decorrelation of diffusive structures is primarily because diffusion occurs on a smaller time scale compared to advective structures.

Correlation of the fields Λ and Ψ with interfaces would show up as (sharp) jumps in their conditional averages at $s = 0$. To highlight the differences and similarities of $\tilde{\Lambda}_T$ and $\tilde{\Psi}_T$ at $\tilde{T} = -1.3$ (the tilde symbol refers to a scaled form), they are shown normalized in figure 11(d,e); their asymptotes at small s is set to 0 while the value at $\tilde{s} = 0.5$ is set to 1. The correlation of both fields with the turbulent-turbulent interface is slightly stronger than that for the turbulent-nonturbulent interface, but otherwise scaled $\tilde{\Lambda}_T$ and scaled $\tilde{\Psi}_T$ are not significantly different.

We observe that both fields, Λ and Ψ , exhibit large spatial fluctuations. Within the turbulent domain, their conditional averages are an order of magnitude smaller than their typical magnitudes, primarily due to the nature of these structures. Diffusive barriers have bounded shapes, while advective barriers form elongated structures that align with the main advection direction (i.e., the streamwise direction). Both structures are represented by a scalar field, where the scalar value remain close to zero in regions without any barriers, even within the turbulent domain. This significantly reduces the conditional average values, with a greater effect on the conditional averages of the diffusive barriers.

D. Diffusive momentum flux

While Ψ_{-T} gauges the convergence properties of the averaged vector field $\bar{\mathbf{b}}_t^{t_0-T}$, such that it is large on lines to which $\bar{\mathbf{b}}_t^{t_0-T}$ is tangent, the diffusive flux through the interface can also be measured directly. Conditional averages of the normal flux $b_\perp = \bar{\mathbf{b}}_t^{t_0-T} \cdot \mathbf{e}_{\text{tnti}}$, and its tangential component $b_\parallel = \bar{\mathbf{b}}_t^{t_0-T} \cdot \mathbf{t}_{\text{tnti}}$, with $\mathbf{t} \perp \mathbf{e}$, are shown in Fig. 12(b,c), respectively.

A striking observation is that the tangential component of the diffusive flux b_\parallel is concentrated in the diffusive superlayer. The width of this superlayer is comparable to the Taylor microscale; see Sec. III. The tangential flux remains comparably invariant in time, with the momentum gradient alight with the flow direction. From the finite-time normal diffusive flux through the interface, we observed negative flux upon entering the interface, suggesting that viscous diffusion transports momentum in a way that the interface grows and propagates into the irrotational domain, and is *not* a tangency line of $\bar{\mathbf{b}}_t^{t_0-T}$. However, unlike the tangential flux, the normal flux is not invariant in time; it increases as the integration time of the Lagrangian diffusive flux increases. These properties are more outspoken for the turbulent-turbulent interface, as shown in figure 12(d,e). The fluctuation amplitudes of these fluxes increase with increasing integration time. This may explain the diminishing

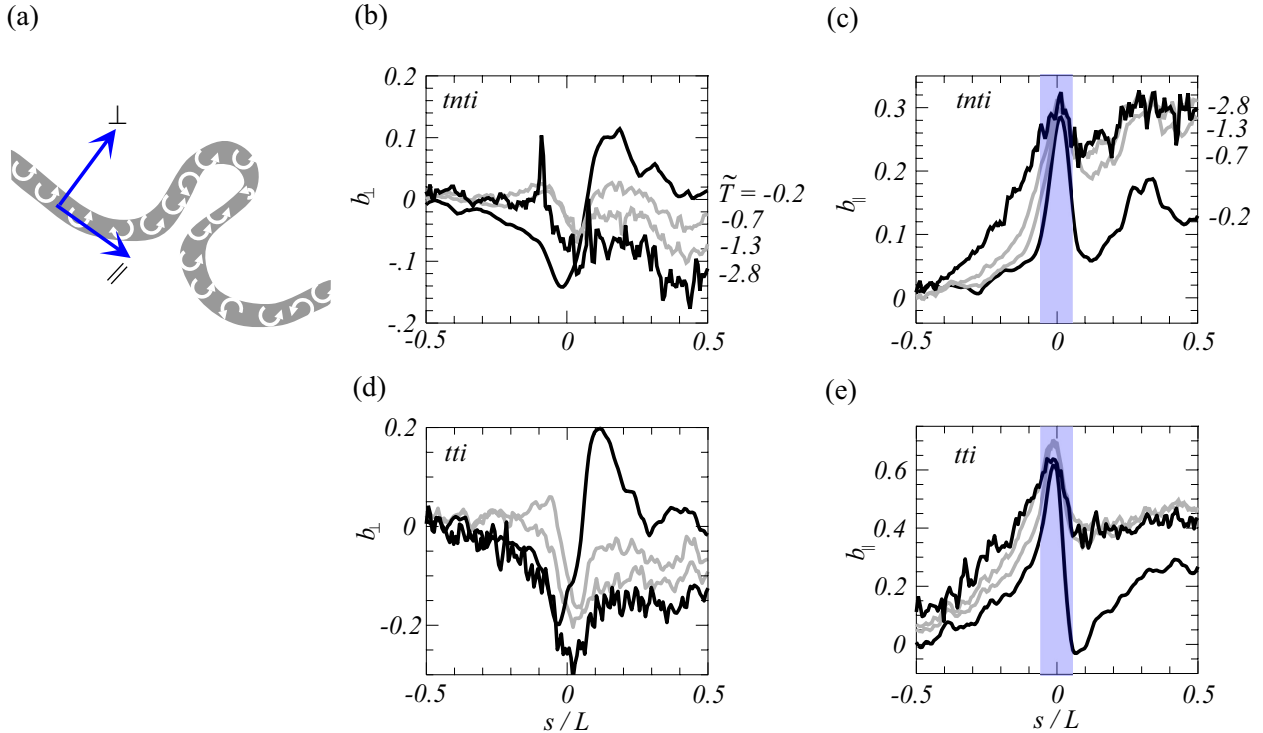


FIG. 12. (a) Cartoon illustrating the diffusive flux normal (\perp) and tangential (\parallel) to an interface. (b) Conditional average of diffusive flux $b_{\perp} = \bar{\mathbf{b}}_{t_0}^{t_0-T} \cdot \mathbf{e}_{\text{tnti}}$ normal to the turbulent-nonturbulent interface interface, for integration times $\tilde{T} = -0.2, \dots, -2.8$. (c) Conditional average of the flux $b_{\parallel} = \bar{\mathbf{b}}_{t_0}^{t_0-T} \cdot \mathbf{t}_{\text{tnti}}$ parallel to the turbulent-nonturbulent interface interface. The width of the blue vertical box indicates the Taylor microscale $\tilde{\lambda}$. (d, e) Same as (b, c), but for the turbulent-turbulent interface.

correlation of Ψ_{-T} with the interfaces.

VII. CONCLUSIONS

We investigate the transport mechanisms of turbulent advection and viscous diffusion, as shaped by turbulent interfacial layers, with the outermost one the turbulent-nonturbulent interface. High spatial resolution and long observation times are achieved in an experimental setup where the field of view moves with the interface, providing quasi-Lagrangian information.

Objectively, we have identified edges in a turbulent velocity field from the distribution of an advected passive scalar. These edges, be it the interface between turbulence and the surrounding quiescent fluid or an internal edge in the turbulent domain, act as shear layers with an associated concentration of vorticity. The surprise is that this works with a rather arbitrary choice of the number of concentration clusters (here $n_c = 4$). Other works [5, 28, 42] also find these edges, but using contours of vorticity or enstrophy instead of scalar concentration.

Our findings show that the intensity of Lagrangian advective and diffusive terms correlate with the interfacial layers. However, these correlations diminish as the integration time T

increases, with barriers to viscous flux decorrelating faster than advective barriers. Most probably, this difference arises because viscous diffusion is a small-scale process, whereas advection occurs on larger scales. Therefore, these Lagrangian structures should decorrelate over shorter times as their scale decreases. This is in accordance with the interpretation of ridges of the finite-time Lyapunov exponent (FTLE) field that block large-scale momentum transport, and the diffusive barrier field whose maxima block diffusive momentum flux.

Our experiment, where we move with the flow, allows us to study the influence of the observation time T . Remarkably, averaging over longer times T results in noisier curves (see Fig. 12). Perhaps longer Lagrangian trajectories encounter more large gradients.

A caveat is that our analysis is two-dimensional as it is based on 2D planar measurement of the velocity and scalar fields. Over one large-eddy turnover time, Lagrangian tracks may wander away from the measured plane, leading to inevitable decorrelation.

The diffusive flux at the interface agrees with the idea of so-called ‘nibbling’ where the turbulent domain grows outward through viscous diffusion transport of vorticity and is illustrated vividly in Fig. 12 persistent flux as time progresses. The diffusive flux parallel to the turbulent-nonturbulent interface is localized within a superlayer whose width is comparable to the Taylor microscale and remains relatively invariant over time.

ACKNOWLEDGMENTS

We acknowledge the support and expertise of Ing. Edwin Overmars in performing the PIV and LIF measurements.

-
- [1] S. Corssin and A. L. Kistler, *Free-stream boundaries of turbulent flows*, Tech. Rep. 1244 (NACA Tech. Note, 1955).
 - [2] C. D. Meinhart and R. J. Adrian, On the existence boundary layer of uniform momentum zones in a turbulent boundary layer, *Phys. Fluids* **7**, 694 (1995).
 - [3] R. J. Adrian, C. D. Meinhart, and C. D. Tomkins, Vortex organization in the outer region of the turbulent boundary layer, *J. Fluid Mech.* **422**, 1 (2000).
 - [4] T. Ishihara, Y. Kaneda, and J. Hunt, Thin shear layers in high Reynolds number turbulence - DNS results, *Flow, Turbul. and Combust.* **91**, 895 (2013).
 - [5] J. Eisma, J. Westerweel, G. Ooms, and G. E. Elsinga, Interfaces and internal layers in a turbulent boundary layer, *Phys. Fluids* **27**, 055103 (2015).
 - [6] J. Westerweel, C. Fukushima, J. M. Pedersen, and J. C. R. Hunt, Mechanics of the turbulent-nonturbulent interface of a jet, *Phys. Rev. Lett.* **95**, 174501 (2005).
 - [7] C. B. da Silva, J. C. R. Hunt, I. Eames, and J. Westerweel, Interfacial layers between regions of different turbulence intensity, *Ann. Rev. Fluid Mech.* **46**, 567 (2014).
 - [8] J. Mathew and A. J. Basu, Some characteristics of entrainment at a cylindrical turbulence boundary, *Phys. Fluids* **14**, 2065 (2002).
 - [9] J. Westerweel, C. Fukushima, J. M. Pedersen, and J. C. R. Hunt, Momentum and scalar transport at the turbulent/non-turbulent interface of a jet, *J. Fluid Mech.* **631**, 199 (2009).

- [10] D. Mistry, J. Philip, J. R. Dawson, and I. Marusic, Entrainment at multi-scales across the turbulent/non-turbulent interface in an axisymmetric jet, *J. Fluid Mech.* **802**, 690 (2016).
- [11] D. Mistry, J. Philip, and J. R. Dawson, Kinematics of local entrainment and detrainment of a turbulent jet, *J. Fluid Mech.* **871**, 896 (2019).
- [12] J. Chen and O. R. H. Buxton, Spatial evolution of the turbulent/turbulent interface in a cylinder wake, *J. Fluid Mech.* **969**, A4 (2023).
- [13] G. Haller and G. Yuan, Lagrangian coherent structures and mixing in two-dimensional turbulence, *Physica D: Nonlinear Phenomena* **147**, 352 (2000).
- [14] S. C. Shadden, F. Lekien, and J. E. Marsden, Definition and properties of lagrangian coherent structures from finite-time lyapunov exponents in two-dimensional aperiodic flows, *Physica D: Nonlinear Phenomena* **212**, 271 (2005).
- [15] G. Haller, Lagrangian coherent structures, *Annu. Rev. Fluid Mech.* **47**, 137 (2015).
- [16] G. Haller, S. Katsanoulis, M. Holzner, B. Frohnapfel, and D. Gatti, Objective barriers to the transport of dynamically active vector fields, *J. Fluid Mech.* **905**, A17, 1 (2020).
- [17] J. Reijtenbagh, J. Westerweel, and W. van de Water, Large-scale structures of scalar and velocity in a turbulent jet flow, *Phys. Rev. Fluids* **6**, 084611 (2021).
- [18] C. Meneveau and K. R. Sreenivasan, Interface dimension in intermittent turbulence, *Phys. Rev. A* **41**, 2246 (1990).
- [19] J. S. Turner, Turbulent entrainment, *J. Fluid Mech.* **173**, 431 (1986).
- [20] L. S. G. Kovaszny, Structure of the turbulent boundary layer, *Phys. Fluids Suppl.* **10**, 25 (1967).
- [21] L. S. G. Kovaszny, V. Kibens, and R. F. Blackwelder, Large-scale motion in the intermittent region of a turbulent boundary layer, *J. Fluid Mech.* **41**, 283 (1970).
- [22] W. C. Reynolds, Large-scale instabilities of turbulent wakes, *J. Fluid Mech.* **54**, 481 (1972).
- [23] M. Holzner and B. Lüthi, Laminar superlayer at the turbulence boundary, *Phys. Rev. Lett.* **106**, 134503 (2011).
- [24] T. Watanabe, Y. Sakai, N. Nagata, Y. Ito, and T. Hayase, Enstrophy and passive scalar transport near the turbulent/non-turbulent interface in a turbulent planar jet flow, *Phys. Fluids* **26**, 105103 (2014).
- [25] G. K. Batchelor, *An Introduction to Fluid Mechanics* (Cambridge University Press, Cambridge, 1967).
- [26] V. Kolár, Vortex identification: New requirements and limitations, *Int. J. Heat Fluid Flow* **28**, 638 (2007).
- [27] K. Chauhan, J. Philip, C. M. De Silva, and N. Hutchins, The turbulent / non-turbulent interface and entrainment in a boundary layer, *J. Fluid Mech.* **742**, 119 (2014).
- [28] M. Asadi, M. Kamruzzaman, and R. J. Hearst, The effect of inlet turbulence on the quiescent core of turbulent channel flow, *J. Fluid Mech.* **A37**, 935 (2022).
- [29] J. C. Bezdek, A convergence theorem for the fuzzy isodata clustering algorithms, *IEEE Trans Pattern Anal Mach Intell* **2**, 1 (1980).

- [30] D. S. Fan, J. L. Xu, M. X. Yao, and J. P. Hickey, On the detection of internal interfacial layers in turbulent flows, *J. Fluid Mech.* **872**, 198 (2019).
- [31] M. E. Gurtin, E. Fried, and L. Anand, *The Mechanics and Thermodynamics of Continua* (Cambridge University Press, Cambridge, 2013).
- [32] P. E. Dimotakis, The mixing transition in turbulent flows, *J. Fluid Mech.* **409**, 69 (2000).
- [33] N. R. Panchapakesan and J. L. Lumley, Turbulence measurements in axisymmetric jets of air and helium. part 1. air jet, *J. Fluid Mech.* **246**, 197 (1993).
- [34] R. J. Adrian and J. Westerweel, *Particle Image Velocimetry* (Cambridge University Press, 2011).
- [35] S. Er, J. P. Laval, and J. C. Vassilicos, Large-scale spectral depletion in turbulent channel flows, *J. Fluid Mech.* **960**, A37 (2023).
- [36] W. J. A. Dahm and P. E. Dimotakis, Measurements of entrainment and mixing in turbulent jets, *AIAA J.* **25**, 1216 (1987).
- [37] B. W. Silverman, *Density Estimation for Statistics and Data Analysis*, Monographs on Statistics and Applied Probability (Chapman and Hall, London; New York, 1986) p. 175.
- [38] P. Bourke, Conrec: A contouring subroutine, *Byte* **12**, 143 (1987).
- [39] R. R. Prasad and K. R. Sreenivasan, Scalar interfaces in digital images of turbulent flows, *Exp. Fluids* **7**, 259 (1989).
- [40] D. K. Bisset, J. C. R. Hunt, and M. M. Rogers, The turbulent/non-turbulent interface bounding a far wake, *J. Fluid Mech.* **451**, 383 (2002).
- [41] D. Mistry, J. R. Dawson, and A. R. Kerstein, The multiscale geometry of the near field in an axisymmetric jet, *J. Fluid Mech.* **838**, 501 (2018).
- [42] M. Holzner, A. Liberzon, M. Guala, A. Tsinober, and W. Kinzelbach, Generalized detection of a turbulent front generated by an oscillating grid, *Exp. Fluids* **41**, 711 (2006).